Scaling in the aggregation dynamics of a magnetorheological fluid

P. Domínguez-García,[1,*] Sonia Melle,[2] J. M. Pastor,[3] and M. A. Rubio[1]
[1]*Departamento Física Fundamental, Universidad Nacional de Educación a Distancisa, Senda del Rey 9, Madrid 28040, Spain*
[2]*Departamento Óptica, Universidad Complutense de Madrid, Arcos de Jalón s/n 28037, Madrid, Spain*
[3]*Departamento Ciencia y Tecnología Aplicada a la Ingeniería Técnia Agrícola, Escuela Universitaria de Ingeniería Técnia Agrícolas, UPM, C. Universitaria s/n 28040, Madrid, Spain*
(Received 2 August 2007; published 13 November 2007)

We present experimental results on the aggregation dynamics of a magnetorheological fluid, namely, an aqueous suspension of micrometer-sized superparamagnetic particles, under the action of a constant uniaxial magnetic field using video microscopy and image analysis. We find a scaling behavior in several variables describing the aggregation kinetics. The data agree well with the Family-Vicsek scaling ansatz for diffusion-limited cluster-cluster aggregation. The kinetic exponents z and z' are obtained from the temporal evolution of the mean cluster size $S(t)$ and the number of clusters $N(t)$, respectively. The crossover exponent Δ is calculated in two ways: first, from the initial slope of the scaling function; second, from the evolution of the nonaggregated particles, $n_1(t)$. We report on results of Brownian two-dimensional dynamics simulations and compare the results with the experiments. Finally, we discuss the differences obtained between the kinetic exponents in terms of the variation in the crossover exponent and relate this behavior to the physical interpretation of the crossover exponent.

DOI: 10.1103/PhysRevE.76.051403 PACS number(s): 61.43.Hv, 82.70.Dd, 83.80.Gv

I. INTRODUCTION

Magnetorheological (MR) [1] and electrorheological (ER) [2] fluids have attracted a great deal of attention [3] in the last 20 years due to the dramatic changes in their properties that occur under the action of external fields. MR and ER fluids are colloidal dispersions of micrometer-sized polarizable particles in some carrier fluid with medium to low viscosity. The key point in MR and ER fluids is that, under the action of an appropriate external field (magnetic or electric, respectively) the particles acquire a nonpermanent dipole moment. Due to the interaction among these dipole moments, the particles aggregate into chainlike structures [4] that induce huge changes in the mechanical and optical properties of the fluid. For instance, viscosity may be increased by a factor of 10^6, and strong optical anisotropy (birefringence and/or dichroism) may appear.

Moreover, because the dipole moment is not permanent, removing the external field turns off the dipolar interaction among particles, so that the aggregates dissolve by particle Brownian motion, and the fluid returns to a nonaggregated configuration. Consequently, the changes induced by the field in the macroscopic properties of the fluid are reversed.

Obviously, the possibility of controlling the macroscopic properties of a fluid by means of an external electromagnetic field has great potential for its use in practical applications. In this respect, MR fluids appear to be the most useful, because higher dipole moments can be induced, which makes available larger particle-particle interactions and, consequently, stronger mechanical actions and shorter response times. In fact, devices built around MR fluids are currently used in striking applications in disparate fields such as the automotive industry, building antiseismic protection, hanging bridge stabilization, prosthetic bioengineering [5], vibration control systems or clutches [6,7], research on rheological properties of living materials [8–10], biomedical applications [11–14], and, recently, the motion and manipulation of small fluid drops in microfluidics [15,16].

The way these applications are designed is somewhat paradoxical, because most devices involve the modulation (temporary destruction and restoration) of the colloidal stability of the fluid, contrary to most applications of colloidal dispersions, in which maintaining colloidal stability is crucial. Consequently, the kinetics of the aggregation and disaggregation processes in MR and ER fluids are issues of crucial practical importance, because these kinetics govern the turn-on and turn-off response times.

Furthermore, MR or ER fluids are interesting from a fundamental point of view, because they are complex fluids in which the interactions among their microscopic components may be controlled rather well at values slightly above the energy of thermal fluctuations. Hence, MR and ER fluids are a kind of benchmark systems in which statistical mechanical aggregation models can be checked [17].

For instance, the irreversible aggregation of particles and the subsequent formation of complex structures has been investigated theoretically and experimentally during the last two decades. Microparticle aggregation studies have been performed in a variety of physical systems, such as ER fluids [18], which consist of colloids of dielectric polarizable particles dispersed into nonconducting liquids, nonmagnetic particles immersed in a ferrofluid (usually named magnetic holes) [19–22], and magnetorheological fluids, which are made of magnetizable particles dispersed into a nonmagnetic fluid [23–27].

The kinetics of irreversible aggregation is usually described [28] in terms of the evolution of the probability density of clusters of size s at time t, $n_s(t)$, and several statistical variables that can be calculated from $n_s(t)$, such as the num-

*pdominguez@fisfun.uned.es

ber of clusters present at time t, $N(t)$, or the average cluster length $S(t)$. The interesting point is that experiments and numerical simulations show that the evolution of these variables displays power-law behavior, namely, $S(t) \sim t^{z}$, $N(t) \sim t^{-z'}$, and $n_1(t) \sim t^{-\omega}$. The values of these exponents are supposed to be characteristic of the aggregation process.

The success of the Witten-Sander model [17,29] [labeled hereafter as the diffusion-limited aggregation (DLA) model] in reproducing the morphology of aggregates formed by isolated particles that diffuse and aggregate into a single cluster has led to the development of models for the cluster-cluster aggregation problem along similar line. In this spirit, several models have been developed [17], in which particles diffuse to aggregate into clusters that in turn diffuse and aggregate into larger clusters. Most of these models are designed so that they may be implemented in Monte Carlo simulations with different aggregation and/or diffusion rules.

The very first formulations were focused on isotropic cluster-cluster aggregation with both mass-independent and -dependent diffusion coefficients and, most of them, dealing with the fractal dimension of the aggregates [30,31]. Simulations of isotropic cluster-cluster aggregation with mass-independent diffusion [28] allowed the definition of a scaling relationship for the cluster size distribution function:

$$n_s \sim t^{-\omega} s^{-\tau} f(s/t^{z}), \tag{1}$$

with $f(x) \sim 1$ for $x \ll 1$ and $f(x) \ll 1$ for $x \gg 1$. This scaling relationship may also be cast in the form

$$n_s \sim s^{-2} g(s/S(t)), \tag{2}$$

where $g(x) \sim x^{\Delta}$ for $x \ll 1$ and $f(x) \ll 1$ for $x \gg 1$. The exponent Δ is called the crossover exponent and is very relevant in this work.

In this formulation, the characteristic exponents depend on model details such as the mass dependence of the diffusion coefficient [32]. In this spirit, Miyazima and co-workers proposed a model considering oriented anisotropic particles aggregating into rodlike clusters with a mass-dependent diffusion coefficient, namely, $D(s) \sim s^{\gamma}$, where the parameter γ is called the diffusion exponent ($\gamma=0$ means mass-independent diffusion). It was found that the scaling form Eq. (2) did hold for this anisotropic diffusion aggregation model, with kinetic exponent $z'=z=1/(1-\gamma)$ provided that the space dimensionality $d \geq 2$. For the case of a diffusion coefficient inversely proportional to cluster size ($\gamma=-1$), we have $z=1/2$, which is close to the experimental values reported for aggregation of dielectric colloids, $z \sim 0.6$ [18]. A later modification of the model [33] to include hydrodynamic interaction effects through the diffusion coefficient, namely, $D(s)=D_0(\ln s)/s$, gave a different functional dependence of the average cluster size with the following form:

$$S(t) \sim [t \ln S(t)]^{\xi}, \tag{3}$$

with the exponent ξ depending on the dimensionality of the system. For systems with $d \geq 2$, $\xi=0.5$. A cross check with numerical Monte Carlo simulations yielded $\xi \simeq 0.51$, while the effective value of z was $z \simeq 0.61$, in good agreement with the experimental value [18].

Coming back to the experimental studies, there are many experiments dealing with the rheology and properties of MR fluids [34]. However, their aggregation kinetics is still not well understood. The literature concerning experimental kinetic exponents in the case of magnetic interaction between particles has been thoroughly reviewed in Ref. [22]. For the sake of completeness, we will briefly summarize here the main experimental results, obtained by video-microscopy techniques unless otherwise specified.

Let us first state that it is usual to classify the experimental data according to the values of two control parameters: the volume fraction ϕ of particles in the suspension, and the ratio between the magnetic interparticle interaction energy and the thermal energy, λ, defined as

$$\lambda \equiv \frac{W_m}{k_B T} = \frac{\mu_0 m^2}{16\pi a^3 k_B T}, \tag{4}$$

where μ_0 is the vacuum magnetic permeability, m the magnetic moment of the particle, a the radius of the particle, k_B the Boltzmann constant, and T the temperature.

In Ref. [20], the aggregation of sulfonated polystyrene particles with 30 wt % content of iron oxide (located in a thin outer shell) in water was studied. The 3.6-μm-diameter particles were enclosed between glass spacers placed 5 μm apart. The value obtained for the growth exponent was $z=1.7$ at $\lambda=1360$ and $\phi \sim 0.1$. Investigations [35,36] of the aggregation kinetics of paramagnetic nanoparticles ($\sim$11 nm diameter) at $\lambda=4.6$ and $\phi=0.021$ yielded exponent values of $z \sim 0.79$ and $z' \sim 0.67$.

The aggregation kinetics of superparamagnetic microparticles, made of magnetite grains randomly dispersed in a polymer matrix, has been studied too [23,24,26]. In Ref. [24], the aggregation of 1.5-μm-diameter particles with 62 wt % iron oxide content was studied and gave $z'=0.5$, with z' being constant in the range $10 \leq \lambda \leq 100$ and $0.005 \leq \phi_{2D} \leq 0.026$, while z varies so that $0.37 \leq z \leq 0.60$. Conversely, in Ref. [26], studies of 0.6-μm-diameter particles with 27 wt % iron oxide content were reported. The authors found a possible dependence of z on the dipolar interaction strength λ, with $0.45 \leq z \leq 0.75$ (using $\lambda=8.6$, 19, and 34 and $2 \times 10^{-4} \leq \phi \leq 2 \times 10^{-3}$).

Later, Sohn [37], working with particles very similar to those used in Ref. [24] (0.8-μm-diameter particles with 68 wt % iron oxide content), obtained $z \sim 1$ for $3 \leq \lambda \leq 30$ and $0.02 \leq \phi \leq 0.06$. However, the value calculated for z may suffer from insufficient temporal sampling.

Light scattering techniques have also been used in this field. For instance, Martin *et al.* [38] studied the aggregation kinetics of an electrorheological fluid made of 0.7-μm-diameter silica particles dispersed in an organic solvent, by means of small-angle light scattering. At $\lambda \sim 10^4$ and high volume fraction $\sim$11 wt %, a value $z=0.4$ was obtained.

Scattering dichroism studies on magnetorheological fluids similar to those used in Refs. [24,26,37] have also been performed [27]. Provided that lateral aggregation does not occur, the dichroism value can be related [27] to the number of aggregated particles N_a, and a temporal power law was found, such as $N_a \sim t^{\beta}$ with $\beta=0.44$, at low volume fractions.

In this work, a theoretical relationship between the dynamic exponents z and β for $S(t) > 20a$ was proposed. However, the relationship between exponents β and z is dubious, because, as we will show later, the power-law regimes for S and N_a do not occur simultaneously.

All of the above-mentioned experimental studies deal just with the temporal exponents z, z', and/or β. To our knowledge, the validity of the scaling ansatz [Eqs. (1) and (2)] has actually been tested only by Fraden *et al.* [18] (in an ER fluid) and, more recently, by Cernak *et al.* [22].

Cernak *et al.* studied a system of magnetic holes using video microscopy. They measured the exponents z, z', and Δ, and checked the validity of the scaling form Eq. (2). They observed large differences between z and z' when $\Delta > 1.8$ and $z = z'$ when $\Delta < 1.8$, in apparent agreement with predictions from scaling theory [22,28]. The values found for the dynamic exponent z vary approximately from 0.4 to 0.59 (except for very large particles). For low particle size and intermediate and low values of λ, they obtain an average value $z = 0.42 \pm 0.06$.

The magnetic hole system is a very nice experimental model to check for the predictions of scaling theory. However, most magnetorheological fluids oriented toward practical applications imply also effects such as sedimentation and/or complex interaction potentials among particles due to surface charges. Assessing the validity of scaling theory for the aggregation kinetics in such conditions still remains an open problem.

Here, we report on an experimental study of the aggregation kinetics in a magnetorheological fluid made of micrometer-sized superparamagnetic particles dispersed in water. The particles are functionalized with surface carboxylic groups and are denser than the surrounding fluid, and therefore they exhibit sedimentation. In this study, the exponents z, z', β, and Δ are determined using experimental methods (video microscopy and image analysis) and by means of Brownian dynamics simulations. In fact, the exponent Δ is obtained in two independent ways. First, it was determined by means of the behavior of the scaling function $g(x)$ at low values of x. Second, using Eq. (2), it can be seen that the decay of the population of nonaggregated particles, $n_1(t)$, follows a power-law behavior $n_1(t) \sim t^{-\omega}$, so the crossover exponent can be obtained from $\Delta = \omega / z$. The experimental results are compared to results of Brownian dynamics numerical simulations. Both the experimental and the numerical results support the validity of the scaling ansatz Eq. (2).

The paper is organized as follows. After this lengthy introduction, we briefly sketch the Smoluchowski theory for cluster-cluster aggregation in Sec. II. Section III contains the description of the experimental setup, the magnetorheological fluid employed, the image acquisition and processing methods, and the numerical simulation method. The experimental and simulation results are presented in Sec. IV and discussed in Sec. V. Finally, conclusions and suggestions for further work appear in Sec. VI.

II. CLUSTER-CLUSTER AGGREGATION

Von Smoluchowski's theory [39] of cluster-cluster aggregation has been described often [18,26,33] in this context, and we will briefly sketch it here for the paper to be self-contained. This theory considers the kinetics of a system of N initially separated identical particles that aggregate to form clusters, which may themselves aggregate to form larger clusters. This continuous process gives rise to a wide distribution of cluster sizes that is specified by the number of clusters of size s present in the system at time t, $n_s(t)$. The time evolution of the population of size s is ruled by the set of equations

$$\frac{dn_s(t)}{dt} = \frac{1}{2}\sum_{i+j=s} K_{ij} n_i n_j - n_s \sum_{j=1} K_{sj} n_j, \tag{5}$$

where the kernel K_{ij} represents the rate at which clusters of size i and j coalesce to give rise to a cluster of size $s = i + j$. Equation (5) directly shows that only binary aggregation processes are considered, so that it must be applicable only at low concentrations of clusters. Moreover, all details referring to the particular physical system of interest are contained in the reaction kernel K_{ij}. For instance, in the case of diffusion-limited aggregation, K_{ij} is proportional to the product of the cluster cross section and the diffusion coefficient. In the case of aggregation into linear chains, it has been argued [40] that the cluster cross section should be independent of the cluster size.

Several statistical measures are typically used to characterize the kinetics of an aggregation process. For instance, the mass average cluster size $S(t)$ is defined as

$$S(t) = \frac{\sum_s s^2 n_s(t)}{\sum_s s n_s(t)}. \tag{6}$$

It is also possible to define an average length of the cluster, which we will label $l(t)$, as

$$l(t) = \frac{\sum_s s n_s(t)}{\sum_s n_s(t)} = \frac{\sum_s s n_s(t)}{N}, \tag{7}$$

where $N(t)$ is the total number of clusters present in the system at time t. In this framework, these quantities are expected to follow simple temporal power laws, with exponents z, z', and $-z'$, respectively,

$$S(t) \sim t^z, \quad l(t) \sim t^{z'}, \quad N(t) \sim t^{-z'}, \tag{8}$$

and the scaling relationship [Eq. (1) or (2)] is supposed to be valid.

Some relationships between the exponents may be obtained on physical grounds. For instance, it can be shown [28] that mass conservation requires

$$\omega = z\Delta, \quad \tau = 2 - \Delta. \tag{9}$$

Moreover, through Eq. (1) and using mass-dependent diffusion coefficient ($D \sim s^{\gamma}$), the relationship can be obtained [17,32] that $z' = \omega$ if $\Delta < 1$ and $z' = z$ if $\Delta > 1$. Dynamic scaling theory also ascribes a physical meaning to the values of the crossover exponent Δ, so that

$$\Delta = \begin{cases} 2-\tau & \text{if } \gamma > \gamma_c, \\ 2 & \text{if } \gamma < \gamma_c, \end{cases} \tag{10}$$

where γ_c is a critical value that indicates the transition between a regime dominated by binary aggregation events that involve one large and one small cluster ($\gamma < \gamma_c$), and a regime where the small-large and large-large interactions have similar probabilities ($\gamma > \gamma_c$).

III. EXPERIMENTAL AND NUMERICAL METHODS

A. Experimental setup

In the experiments reported here, the MR fluids were surfactant-stabilized aqueous suspensions of superparamagnetic particles, supplied by Estapor (M1-070/60). These particles consist of a polystyrene matrix with embedded magnetite crystals of small diameter (10 nm, typically). Since these iron oxide grains are randomly oriented inside the microparticles, the resulting magnetic moment is zero in the absence of an external magnetic field. The superparamagnetic particles have a diameter of 0.97 μm and a magnetite content of 54.65 wt %, which yields a density of 1.85 g/cm^3.

To avoid particle aggregation and assure redispersion of the particles upon external field switch-off, both a surfactant and charge stabilization are used. Indeed, the surface of the latex microspheres is functionalized with carboxylic groups, and sodium dodecyl sulfate (SDS) is added to the suspension at a concentration of 1 g/l. Variation of the volume fraction of the suspension is achieved by convenient dilution, always keeping the SDS concentration of the resulting suspension at the above-mentioned value.

When an external magnetic field $\vec{H}$ is applied, a net magnetic dipole moment aligned with the external field is induced in the particles. This magnetic moment is $\vec{m} = (4\pi/3)a^3\vec{M}$, with $\vec{M} = \chi\vec{H}$, where $\vec{M}$ is the magnetization of the particle and χ the particle magnetic susceptibility. We have characterized the magnetic properties of the particles by measuring their magnetization curve using a Vibrating Sample Magnetometer (VSM). These measures permit us to obtain the λ value [Eq. (4)] when the magnetic field amplitude is varied. This curve can be seen on Fig. 1; in the inset we show a detail of the central zone. For the particles used in these experiments, a magnetic saturation of 42 kA/m (23 emu/g) is obtained, in agreement with an estimation in the form $M_s \sim 0.54\ M_s^{Fe_3O_4} \sim 27$ emu/g, where 0.54 is the percentage of magnetic content in the particles and $M_s^{Fe_3O_4} = 49$ emu/g is the magnetic saturation of magnetite [41]. In the inset of Fig. 1 a small hysteresis loop is observed. Making an average value for the two branches of the curve in the range $|H| < 10$ kA/m, a magnetic susceptibility value $\chi \sim 1.6$ is obtained, in agreement with the value $\chi \sim 1.5$ reported in Ref. [24] with similar particles.

The suspension sample is confined in a cylindrical cell made of two horizontal quartz windows and a Teflon spacer with inner diameter 6.5 mm and height 100 μm. The whole system is placed inside a chamber surrounded by a circulating thermostatic bath that keeps the temperature constant during the experiments at $T = 282$ K. Each of the experiments reported here is performed on a freshly prepared MR fluid sample.

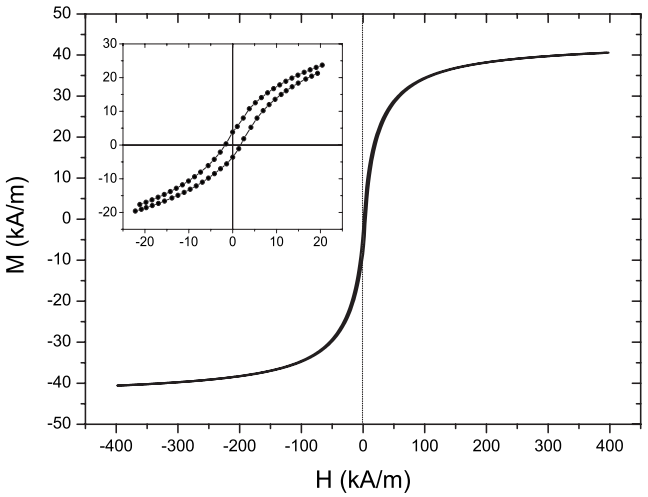

FIG. 1. Magnetization curve for the magnetic particles used in this work with a magnetic saturation $M_s = 42$ kA/m. Inset: Detail of the central region of the curve ($|H| < 20$ kA/m), showing the presence of a small hysteresis loop.

The system used to generate the magnetic field has been thoroughly described elsewhere [42]. Briefly, it consists of two orthogonal pairs of coils driven by two computer-controlled arbitrary function generators (HP-33120A) that feed two high-power amplifiers (Kepco, BOP50-4M and BOP50-2M). That system allows the generation of highly uniform time-varying magnetic fields, with a spatial variation of the magnetic field lower than 0.3% in the observed region. Nevertheless, in the present experiments, only uniaxial stationary magnetic fields are employed, so that only one function generator, one amplifier, and a pair of coils are used. The generated magnetic field is set perpendicular to the vertical axis of the experimental cell.

The video-microscopy setup used to grab the images is located below the sample, and is formed by a Navitar long-working-distance microscope with zoom capabilities attached to a digital charge-coupled device camera (Retiga EX), with a spatial resolution of 1360×1036 pixels, 12-bit intensity resolution, and a maximum acquisition speed of one full frame image every 0.3 s (see Fig. 2).

As stated above, the particles are denser than the carrier fluid and, therefore, they sediment toward the bottom cell wall. The sedimentation takes place in a time ruled by the sedimentation velocity $U_s = MgD_0/k_BT(1-\rho/\rho_p) \sim 0.23$ μm/s, where M is the mass or the particle, D_0 the particle's diffusion coefficient in water, ρ the water density, and ρ_p the particle density. In the experimental conditions, D_0 can be estimated by means of the Stokes-Einstein relation to be $D_0 = k_BT/6\pi\eta a = 0.343$ μm^2/s. Hence, the time needed for a particle at the middle of the cell to settle to the equilibrium layer (48.5 μm) is ~140 s. In all of the experiments here reported we waited for about 15 min before starting the experiment, in order to make sure that the suspension is settled.

Assuming that the Boltzmann density profile is a reasonable approximation for the real density profile [43], it can be

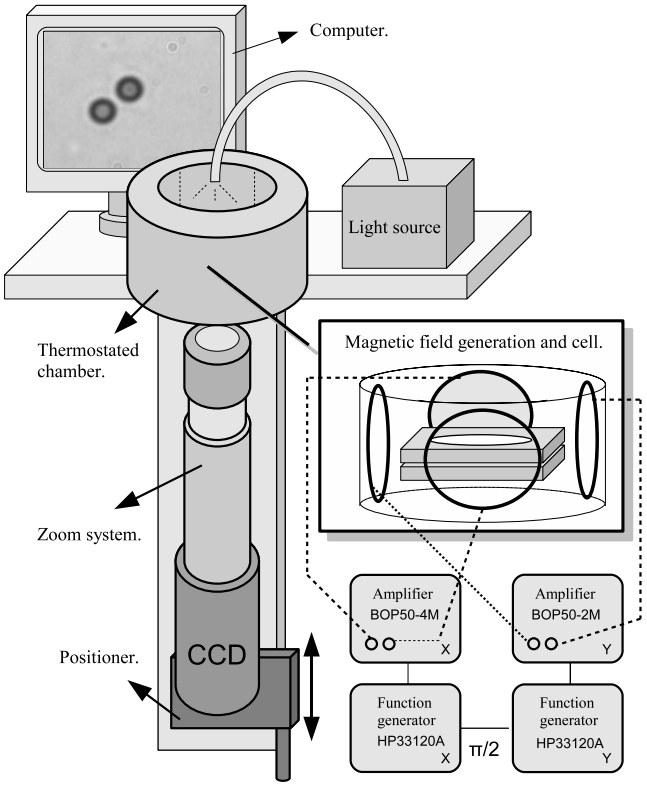

FIG. 2. Scheme of the video-microscopy setup. In the inset we show an outline of the cell that contains the MR fluid and the system for generating the magnetic field.

estimated that 85% of the particles in the dispersion lie in a thin bottom layer with a thickness of 2 particle diameters. For our experimental conditions, it can be calculated that the particles are situated an average distance of ~ 1 μm above the bottom window.

The experimental procedure is as follows. Once the sample cell containing the magnetic suspension is introduced in the experimental setup, it is left to stand for at least 15 min free of applied magnetic field for the particles to sediment. In that way, the magnetic particles have enough time to settle to the Boltzmann equilibrium density profile. Therefore, the system of particles is quasi-two-dimensional (quasi-2D) and, consequently, we focus the imaging system on the layer of particles located right above the bottom quartz window. After this rest period, we capture typically 5 min of images without field. Images are captured at a rate of one every 0.4 s, at maximum spatial resolution. Then we apply a constant uniform magnetic field for 5000 s, typically. Therefore, each experiment comprises about 18 000 images that are stored in real time on the hard disk of the controlling computer for later processing. This procedure has been performed in experiments carried out at different values of λ and surface fraction ϕ_{2D}.

Image analysis, data extraction, and statistical calculations have been carried out with our own developed software, based on the free open-source Java program for image analysis named IMAGEJ [44]. In this software, we implement an adaptive threshold algorithm. Briefly, the software removes the image background and captures adequately the contour

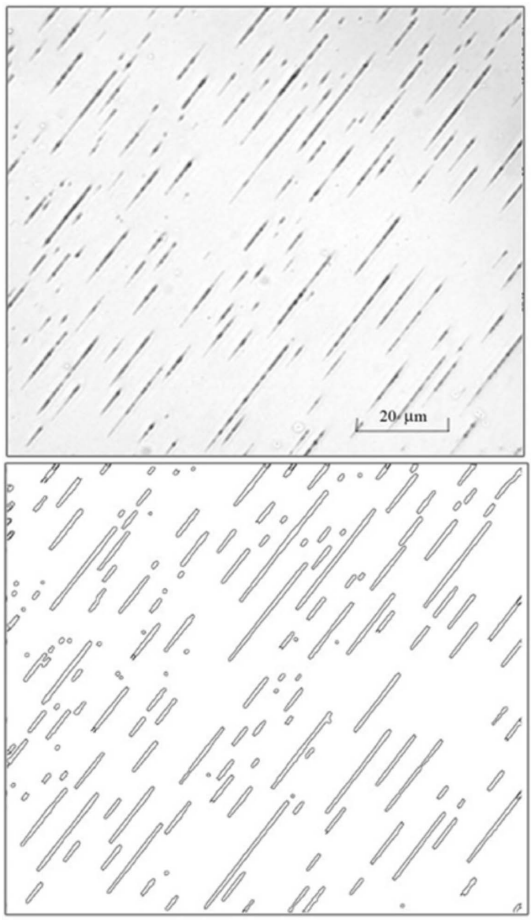

FIG. 3. Video-microscopy image showing the clusters formed by the microparticles after $t=4358.4$ s of constant applied field with $\lambda=1718$, $\phi_{2D}=0.088$. Top: original captured image. Bottom: corresponding analyzed binary image.

of the clusters. An example can be seen in Fig. 3: in the top image, we show the original captured image and on the bottom we show the analyzed binary image.

From the series of images, we are interested in obtaining the evolution of relevant physical variables. The image analysis detects only the contour of the clusters from the images, and it is possible to obtain the number of clusters, N, as well as the mean cluster size, $S(t)$, directly from the contour of the objects. However, this is not possible for the number of free or nonaggregated particles (isolated particles), $n_1(t)$, nor for the number of aggregated particles (number of particles forming clusters), $N_a(t)=\Sigma_{i\geq 2} s n_s(t)$, where the number of particles composing the cluster is needed. The easiest way to make that calculation is to divide the area of the individual objects found by the algorithm by the area of an individual particle. The results of this procedure upon the experimental images are not very good, because both the polydispersity of the particles and their Brownian motion in the direction perpendicular to the bottom glass plate introduce large dispersion in the distribution of apparent particle area.

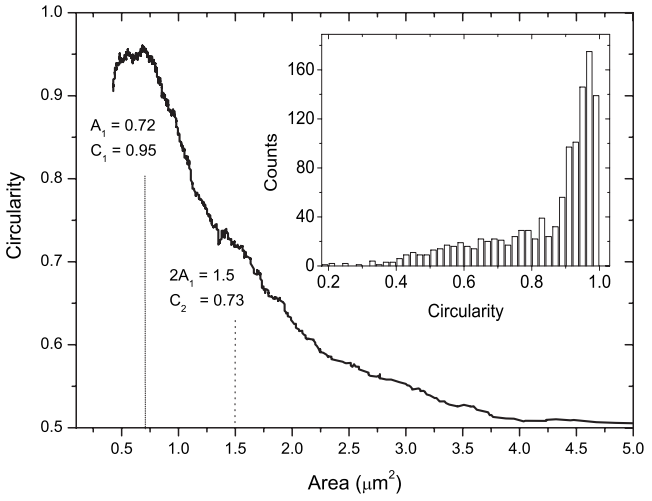

FIG. 4. Circularity vs area for an experiment with ϕ_{2D} without magnetic field for estimating the doublet circularity C_2. Inset: circularity histogram. 76% of the objects are contained in the range $0.8 \leq C \leq 1$.

Therefore, in order to distinguish isolated particles from chainlike clusters, we have implemented a circularity criterion. The circularity of an object can be defined as $C \equiv 4\pi A/P^2$, where P and A are the perimeter and the area of the object, respectively. Obviously, a circle has $C=1$; any other planar geometrical shape yields a lower circularity value. In the case of interest here, it is obvious that the circularity of linear chains decreases with increasing number of particles in the chain, with doublets having the highest circularity among all chains. Consequently, the implementation of the criterion is quite simple: if the circularity of an object is greater than the circularity of a doublet, the object is considered an isolated particle. To calculate the value for the circularity threshold, we estimate the expected area of a doublet as twice the area of one particle, using the calibrated magnification of the imaging system. Then, we keep the circularity values that correspond to doublets whose area is close to the expected one. These selected circularity values are used to compute an average doublet circularity, as can be seen in Fig. 4. This procedure is repeated for several images taken with no magnetic field, and a further averaged value is obtained for the doublet circularity.

B. Numerical model

The experimental results have been compared to numerical simulations of a simple model for a MR fluid. For that purpose, we performed 2D Brownian dynamics (BD) simulations of a system of monodisperse hard spheres interacting through dipolar magnetic interactions and subject to Stokes friction against the carrier fluid [42]. Several approximations have been made in order to keep computational complexity to a minimum. For instance, inertia terms in the equation of motion have been neglected because the Reynolds number for the particle's motion is guaranteed to be very small ($\mathrm{Re} \leq 10^{-4}$). Local field corrections to the magnetic field and hydrodynamic interactions (particle-particle and particle-wall) have been disregarded too.

Considering the previous assumptions, the Newton equation of motion reads, in dimensionless form,

$$\frac{d\vec{R}_i}{d\tau} = \frac{t_s}{2a\gamma_0} \sum_{i \neq j} \vec{F}_{ij}, \tag{11}$$

where $\gamma_0 = 6\pi\eta a$ is the Stokes friction coefficient, the dimensionless position vector of the ith particle is $\vec{R}_i = r_i/2a$, $t_s \equiv 12^2\eta/\mu_0 M^2$, $\tau = t/t_s$ is the dimensionless time, and $\vec{F}_{ij}$ is the total force exerted by the jth particle onto the ith particle. The term $\vec{F}_{ij}$ contains contributions of three types, namely, the magnetic force $\vec{F}_{ij}^{m}$ that drives the aggregation process, an excluded-volume force $\vec{F}_{ij}^{\mathrm{EV}}$ that prevents particle overlap, and a Brownian term $\vec{F}_{ij}^{B}$. To represent the magnetic force, we use the point-dipole approximation

$$\vec{F}_{ij}^{m} = \frac{3\mu_0 m^2}{4\pi} \sum_{i \neq j} \frac{1}{r_{ij}^4} \{[1 - 5(\hat{m} \cdot \hat{r}_{ij})^2]\hat{r} + 2(\hat{m} \cdot \hat{r}_{ij})\hat{m}\} \tag{12}$$

where $\vec{r}_{ij} = \vec{R}_i - \vec{R}_j$, $\hat{r}_{ij} = \vec{r}_{ij}/r_{ij}$ is the unitary vector between the centers of mass of particles i and j, and $\hat{m} = \vec{m}/m$ is the unitary vector corresponding to the magnetic dipole moment, which is considered to be aligned with the field direction for all particles when the local field correction to the magnetic field is neglected. The excluded-volume force is a short-range force that increases sharply when the particles come into contact. We use the expression [45,46]

$$\vec{F}_i^{\mathrm{EV}} = A \frac{3\mu_0 m^2}{4\pi(2a)^4} \sum_{i \neq j} \exp[-B(r_{ij}/2a - 1)]\hat{r}_{ij}, \tag{13}$$

where the parameters A and B have been set as $A=2$ and $B=10$, so that for two particles that are in mechanical contact, the repulsive force exactly balances the attractive dipolar magnetic interactions. The thermal fluctuations can be included, adding the following term:

$$\langle F_{il}^{B}(t) F_{i'l'}^{B}(t') \rangle = 2D\delta(t - t')\delta_{ii'}\delta_{ll'}, \tag{14}$$

where D is the particle diffusion coefficient and the subscript l corresponds to the spatial directions, $l = x,y,z$.

The control parameters in the simulations are λ and ϕ_{2D}. The value of λ is set directly, while the value of ϕ_{2D} is set by choosing the size L of the square box occupied by the system. Then, the number of particles is set to $N_p = \phi_{2D} L^2/\pi a^2$, and the initial average distance between particles is $l \sim 2a(\phi_{2D})^{-1/2}$. The ranges of values of the control parameters used in the simulations were $100 \leq \lambda \leq 3000$, $0.03 \leq \phi_{2D} \leq 0.15$, and $L = 200$, 300, 500, which gave runs with numbers of particles in the range $1521 \leq N_p \leq 17\,161$.

The initial condition for the simulations was prepared by, in the first place, placing the particles in a regular square lattice with step l; second, imposing random displacements of modulus smaller than $(l-2a)/2$ (to avoid overlapping) on the positions of the particles; and running the simulation with $\lambda = 0$, i.e., allowing for pure diffusion of the particles, during a time of the order of $10l^2/D_0$. In the analysis of the simu-

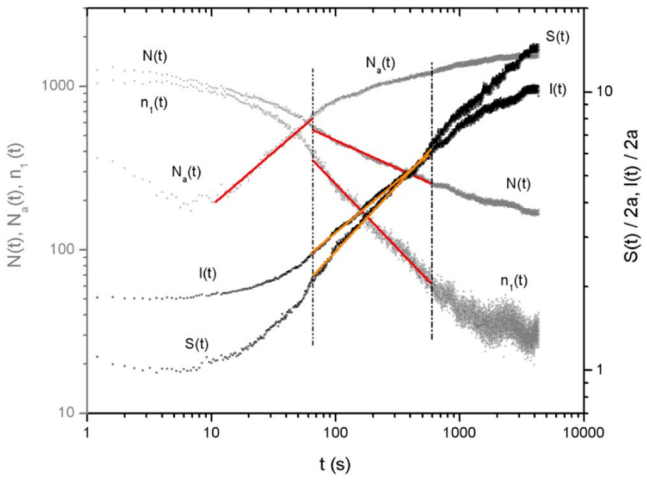

FIG. 5. (Color online) Typical example of the evolution of the kinetic variables at $\lambda=1718$, $\phi_{2D}=0.088$. On the left axis (gray points) $N(t)$, $N_a(t)$, and $n_1(t)$ are represented. Dimensionless values of $S(t)$ and $l(t)$ are represented on the right axis (black points). The vertical lines indicate the region of power-law behaviors [except for $N_a(t)$]. See the values obtained for the exponents in Table I.

lation results, we have employed the following aggregation criterion: two nearby particles are considered to be aggregated if the separation between their closest surface elements is smaller than 10% of the particle diameter. This criterion closely resembles the one used for the experimental images. The time step in the numerical simulations was 0.001 in dimensionless units, which proved to be small enough to avoid strong accelerations due to significant overlapping when the particles came into close contact.

IV. RESULTS

A. Experimental results

Every image acquired during the experiment is stored in real time on the hard disk of the computer that controls the experiment. After the experiment is finished, all of the images are processed by means of the cluster recognition program, which yields a list of clusters and their contours. These lists are further processed to compute the statistics of the different relevant physical magnitudes, namely, the number of clusters in the image, $N(t)$, the average cluster size $S(t)$, the average chain length $l(t)$, the number of aggregated particles, $N_a(t)$, and the number of isolated particles, $n_1(t)$. Typical experimental results for all of these magnitudes are shown in Fig. 5. In this case, the experiment was run at $\lambda=1718$, and $\phi_{2D}=0.088$. On the right axis we represent the dimensionless values of $S(t)$ and $l(t)$ using the diameter of the particle, while in the left axis we represent $N(t)$, $N_a(t)$, and $n_1(t)$.

In Fig. 5, several facts can be appreciated that show up consistently in all of the experiments we have carried out. First of all, it should be noticed that, at the initial time, the total number of clusters is larger than the number of isolated particles, $N(0)>n_1(0)$, and that the number of aggregated particles is not null. This is due to the limited resolution in the recognition of isolated particles. In fact, at the very beginning, a small fraction of the particles are counted as doublets, because of the limited resolution for small objects, so that $N(0)=n_1(0)+N_a(0)/2$. Moreover, the subsequent evolution of N_a shows a decrease to a minimum value of approximately $N_a(0)/2$. This happens because the pairs of nearby particles that are initially counted as doublets are oriented randomly with respect to the magnetic field. Now, the dipolar magnetic interaction between a pair of particles is attractive if the angle between the vector that links the particle centers and the magnetic field, θ, is $\theta\leq\theta_c=\arccos(1/\sqrt{3})\sim 55°$, and repulsive otherwise. Therefore, the initial doublets that have orientations lying in the attractive region do really aggregate, and remain as doublets, while the initial doublets that have orientations lying in the repulsive region separate and go into two isolated particles. Consequently, a fraction of the initial doublets of the order of $2\theta_c/\pi\sim 60\%$ will remain as doublets, while approximately 40% of the initial doublets will separate into isolated particles.

All of the quantities plotted here show some region in which power-law behavior is observed. It is important to notice that $N(t)$, $S(t)$, $l(t)$, and $n_1(t)$ share a common region of power-law behavior; this region is indicated in Fig. 5 by two vertical lines. On the other hand, the number of aggregated particles, $N_a(t)$, displays power-law behavior at shorter times. A closer inspection of the data shows that the region in which $N_a(t)$ displays power-law behavior corresponds to a regime that is dominated by the aggregation of pairs of isolated particles into doublets, and where very few clusters of size larger than two particles are formed.

The exponents for $N(t)$, $S(t)$, $l(t)$, and $n_1(t)$ are calculated for the data within the common region of power-law behavior. The results for all of the experiments, together with the exponent of $N_a(t)$, are reported in columns 3–7 of Table I. The uncertainty in the reported values is one unit in the least significant figure, except for the two last columns, where calculation is straightforward once we know the uncertainties for ω, z, and z'. We would like to remark that the values of z' obtained from $N(t)$ and $n_1(t)$ are in agreement within the experimental error.

A complete check of the scaling ansatz [Eq. (2)] requires a study of the fit of the scaling function to the experimental results, and we also need to obtain the crossover exponent Δ [18,22]. The scaling function is appropriate for the experiment if the experimental data show good collapse onto a single curve when the function $s^2n_s(t)$ is plotted against $s/S(t)$. If good collapse is obtained, the logarithmic slope of the scaling function at small values of $s/S(t)$ provides the value of Δ. Of course, good collapse should be expected only in the time range in which $S(t)$ shows power-law behavior.

Typical experimental data for the scaling analysis are shown in Fig. 6. The data correspond to the experiment whose evolution is represented in Fig. 5, limited to time values within the region bounded by the two vertical lines. The collapse of the experimental data is remarkable. The logarithmic slope of this plot yields a value of the crossover exponent $\Delta=1.66\pm0.08$. The values obtained for Δ for all experiments, together with their uncertainties, are shown in Table I.

TABLE I. Experimental results.

λ	ϕ_{2D}	R_1/R_0	β	ω	z'	z	ξ	Δ	ω/z
48	0.074	1.12	0.23	0.73	0.47	0.61	0.33	1.2±0.2	1.20
77	0.071	1.28	0.31	0.95	0.49	0.50	0.34	1.94±0.06	1.90
77	0.132	1.74	0.35	1.05	0.55	0.48	0.34	2.3±0.1	2.19
171	0.068	1.64	0.48	1.13	0.57	0.61	0.38	1.77±0.07	1.85
171	0.115	2.13	0.65	0.92	0.51	0.50	0.30	1.7±0.1	1.84
296	0.145	2.87	0.40	1.15	0.57	0.60	0.42	1.8±0.1	1.92
455	0.039	1.71	0.24	0.71	0.40	0.48	0.30	1.6±0.1	1.48
455	0.084	2.52	0.59	1.06	0.46	0.59	0.39	1.7±0.1	1.80
455	0.112	2.91	0.50	0.73	0.44	0.51	0.31	1.5±0.1	1.43
640	0.051	2.19	0.56	1.28	0.54	0.61	0.41	1.9±0.2	2.10
640	0.086	2.85	0.65	1.00	0.45	0.60	0.43	1.43±0.05	1.67
812	0.031	1.87	0.62	1.03	0.48	0.65	0.47	1.6±0.1	1.58
812	0.038	2.06	0.41	0.65	0.41	0.54	0.41	1.6±0.1	1.20
812	0.106	3.43	0.40	1.06	0.49	0.65	0.47	1.60±0.08	1.63
985	0.051	2.54	0.27	0.73	0.38	0.43	0.40	1.4±0.2	1.70
985	0.075	3.08	0.42	0.96	0.50	0.67	0.46	1.3±0.1	1.43
1531	0.059	3.17	0.21	0.74	0.44	0.64	0.44	0.9±0.1	1.16
1718	0.088	4.01	0.66	0.79	0.34	0.48	0.38	1.66±0.08	1.63
1909	0.045	2.97	0.38	0.88	0.41	0.54	0.49	1.7±0.1	1.63
2844	0.043	3.33	0.31	0.82	0.45	0.61	0.44	1.4±0.1	1.34

A cross check of the values of the crossover exponent can be performed directly using the relationship $\Delta=\omega/z$. The resulting values are also summarized in Table I. Good agreement is found between the values shown in the columns labeled Δ and ω/z of Table I.

B. Numerical results

As far as the scaling aspects are concerned, the numerical simulation results show a behavior similar to the experimental one. A typical evolution of the kinetic variables is shown in Fig. 7, obtained with parameter values $\lambda=100$, $\phi_{2D}=0.15$, $L=300$, and $N=17161$.

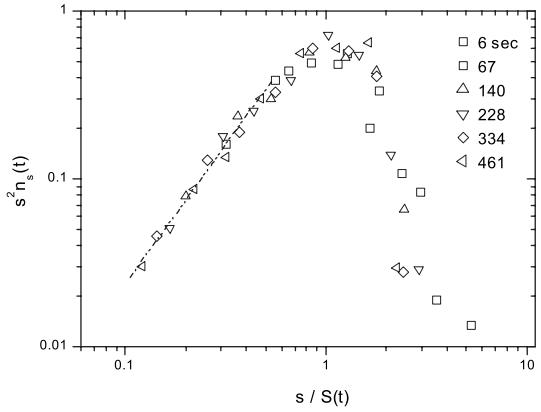

FIG. 6. Experimental representation for the scaling function in the $\lambda=1718$, $\phi_{2D}=0.088$ case. A crossover exponent $\Delta=1.66\pm0.08$ is obtained.

Many common features with the experimental results can be observed. For instance, the power-law regimes for variables $N(t)$, $S(t)$, $l(t)$, and $n_1(t)$ coincide again in the same time region. The power-law region for $N_a(t)$ is also dominated by aggregation of two isolated particles to give a doublet. However, in the simulations large numbers of aggregated particles are achieved comparatively faster than in the

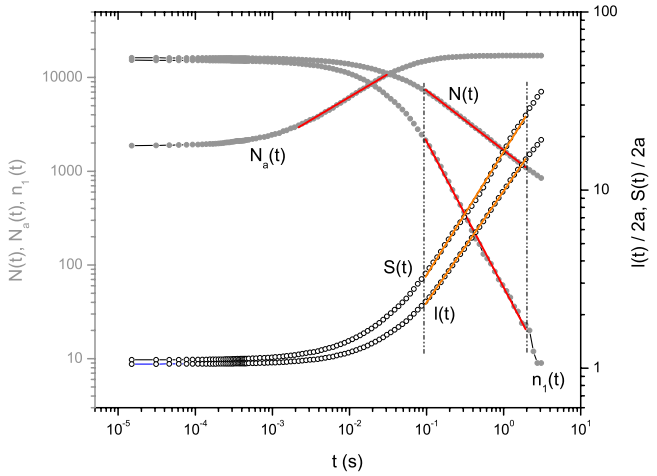

FIG. 7. (Color online) Evolution of the kinetic variables in a typical numerical simulation with parameter values $\lambda=100$, $\phi_{2D}=0.15$, $L=300$, $N=17161$ (the corresponding values for the kinetic exponents are included in Table II). $N(t)$, $N_a(t)$, and $n_1(t)$ are represented on the left axis (filled gray circles). $S(t)/2a$ and $l(t)/2a$ are represented on right axis (black circles). The vertical lines indicate the region of power-law behavior [except for $N_a(t)$].

TABLE II. 2D Brownian dynamics simulation results.

λ	ϕ_{2D}	L	R_1/R_0	N_{part}	ω	β	z'	z	Δ	ω/z
100	0.15	300	2.03	17161	1.57	0.50	0.64	0.69	2.01±0.14	2.26
300	0.03	200	1.31	1521	1.61	0.56	0.56	0.54	2.8±0.2	2.99
300	0.03	500	1.31	9409	1.47	0.54	0.53	0.53	2.40±0.12	2.75
300	0.06	300	1.85	6724	1.42	0.57	0.62	0.67	2.15±0.14	2.12
300	0.09	300	2.27	10201	1.64	0.55	0.64	0.66	2.45±0.11	2.48
300	0.12	300	2.62	13689	1.47	0.53	0.68	0.77	2.06±0.13	1.90
300	0.15	300	2.93	17161	1.50	0.49	0.65	0.66	2.3±0.2	2.27
1000	0.03	200	1.96	1521	1.42	0.57	0.50	0.43	2.90±0.10	3.30
1000	0.03	500	1.96	9409	1.28	0.57	0.53	0.45	2.6±0.2	2.84
1000	0.06	300	2.77	6724	1.58	0.57	0.55	0.53	2.85±0.15	2.98
1000	0.09	300	3.39	10201	1.36	0.55	0.66	0.72	1.95±0.07	1.89
1000	0.12	300	3.91	13689	1.45	0.52	0.65	0.70	2.2±0.3	2.07
1000	0.15	300	4.38	17161	1.52	0.48	0.64	0.73	2.0±0.2	2.08
3000	0.03	200	2.82	1521	1.33	0.53	0.44	0.42	2.51±0.12	3.17
3000	0.06	300	3.99	6724	1.67	0.57	0.63	0.70	2.29±0.11	2.39
3000	0.09	300	4.89	10201	1.54	0.55	0.64	0.69	2.24±0.12	2.23
3000	0.12	300	5.65	13689	1.51	0.51	0.61	0.63	2.0±0.2	2.41
3000	0.15	300	6.31	17161	1.42	0.49	0.65	0.71	2.00±0.15	2.00

experiments, so that the power-law region shrinks.

The kinetic exponents obtained from the simulations performed are shown in Table II. Good agreement is found for exponent z, but the agreement is less good for exponents β and z', and clear discrepancies are found between the values of exponents ω and Δ in experiments and simulations.

A typical result of the scaling analysis on the simulation data is shown in Fig. 8. The exponents have been calculated in the regions $10^{-3} \leq t \leq 10^{-2}$ s, for exponent β, and $0.1 \leq t \leq 1$ s, for exponents ω, z, and z'. The values obtained for Δ for all simulations, together with their uncertainties, are summarized in Table II. The cross check against the values obtained for ω/z is again very satisfactory within the estimated error.

The agreement between the values obtained separately for Δ and ω/z shows unambiguously the validity of their equality. Let us remark that the relation between Δ and ω/z is obtained by imposing the condition of particle number conservation on the scaling relationship [Eq. (2)]. This shows that, within the region where power-law regimes are observed, events consisting of lateral aggregation of isolated particles over long sedimented chains are very rare and are, therefore, statistically irrelevant.

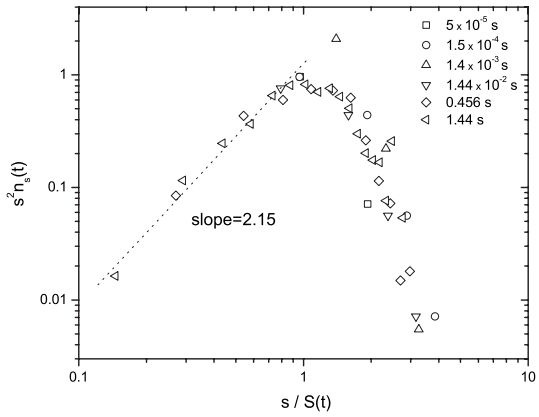

FIG. 8. Scaling analysis for typical simulation data obtained for parameter values $\lambda=300$, $\phi_{2D}=0.06$, $L=300$. A crossover exponent $\Delta=2.15\pm0.14$ is obtained.

V. DISCUSSION

We have not found a direct dependence of the different exponents summarized in Tables I and II with the external parameters λ and ϕ_{2D}. For that reason, in order to compare with the values reported in the literature, we have calculated average values of these exponents over all the exponents, for both experiments and simulations. The results are shown in Table III. The expressed uncertainties are in each case the standard error of the mean. The average experimental value found for the exponent associated with the evolution of the number of aggregated particles, $\langle\beta\rangle=0.43\pm0.02$, is in very good agreement with the value found by means of the scattering dichroism technique [27], namely, $\beta=0.44\pm0.02$, at similar low values of ϕ_{2D}. However, it is somewhat smaller than the value obtained in the simulations, $\langle\beta\rangle=0.50\pm0.02$.

The average values of the exponents $\langle z'\rangle$ and $\langle\omega\rangle$ reflect better the discrepancies between the values obtained in the

TABLE III. Average values of kinetic exponents.

Type	$\langle\beta\rangle$	$\langle\omega\rangle$	$\langle z'\rangle$	$\langle z\rangle$
Experiments	0.43±0.02	0.92±0.04	0.47±0.02	0.57±0.03
Simulations	0.55±0.01	1.5±0.1	0.59±0.01	0.62±0.02

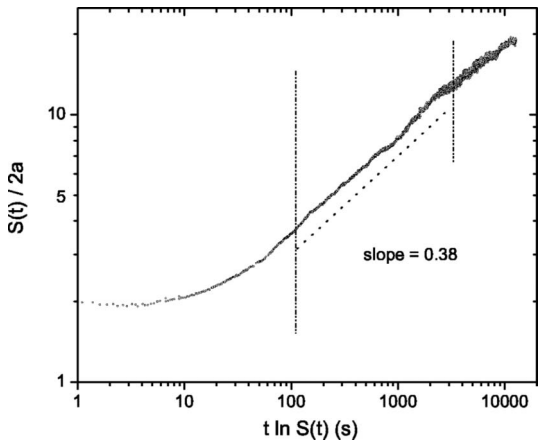

FIG. 9. Experimental representation for the functional dependence of Eq. (3) for the $\lambda=1718$, $\phi_{2D}=0.088$ case. A $\xi=0.38$ exponent is obtained.

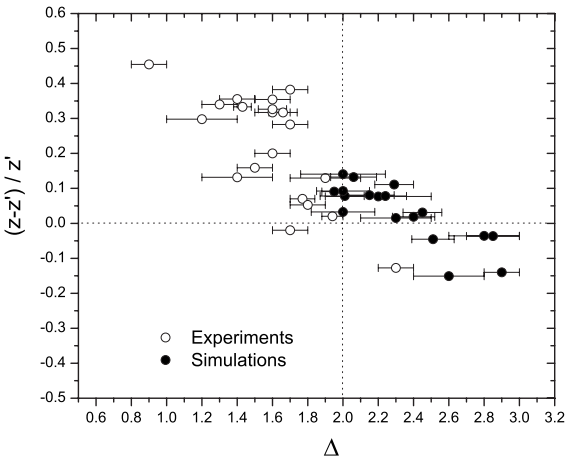

FIG. 10. Relative difference between kinetic exponents, $(z-z')/z'$, versus the crossover exponent values Δ for experiments (empty dots) and for numerical simulations (black dots).

experiments and in simulations. However, the agreement obtained for the $\langle z\rangle$ exponent is rather good. Moreover, the values obtained for $\langle z\rangle$, both in experiments and by simulations, are perfectly compatible with most results yet published, which report values $z\sim 0.60$ for these kinds of system [18,33]. In Ref. [33], it was proposed that values of the z exponent close to 0.6 appear because of the effects of hydrodynamic interactions between particles within the same cluster, leading to a modified power law [see Eq. (3)]. That functional dependence is plotted in Fig. 9 using the data from an experiment with $\lambda=1718$ and $\phi_{2D}=0.088$. Power-law behavior is observed and, for the data in this figure, the exponent obtained is $\xi=0.38$. The values obtained for this exponent are also shown in Table I. The average value obtained for all the experiments gives $\langle\xi\rangle=0.40\pm0.02$. This result is lower than the $\xi\simeq 0.51$ value obtained by Miguel *et al.* but higher than the $\xi\simeq 0.31$ obtained by Cernak *et al.* No systematic dependence of ξ on the values of λ or ϕ_{2D} is observed.

Another discrepancy between experiments and simulations is found in the values of the exponents ω and Δ. It appears that exponents ω and Δ take much larger values in the simulations than in the experiments. While $\langle\omega\rangle_{\text{expt}}=0.92\pm0.04$, the corresponding value for the simulations is $\langle\omega\rangle_{\text{sim}}=1.5\pm0.1$. For the crossover exponent, we notice that the range of values for experiments and simulations is different, so $1\leq\Delta_{\text{expt}}\leq 2\leq\Delta_{\text{sim}}\leq 3$. Both facts may be related to the different behavior of isolated particles in the simulations and in the experiments.

Moreover, the dispersion in the exponent values, both experimentally and numerically, is bigger for ω and Δ, and smaller for z. This probably reflects the relative role of the number of isolated particles in each of the exponents. Indeed, the exponent ω depends entirely on the evolution of the number of isolated particles, while the exponent z, being a second moment of the cluster size distribution, gives much more weight than z' to the population of larger clusters. On the contrary, regarding the number of clusters, $N(t)$, the larger clusters count as much as a single free particle. The evolution of $n_1(t)$ might be very sensitive to the initial spatial configuration of the particles, and neither the experiments nor the simulations have been averaged over realizations. That means that, if the difference between experiments and simulations is related to the free particles, the discrepancies between exponents should be clear for z', ω, and β but not for z, as observed.

With the intention of exploring this possibility, we represent in Fig. 10 the relative difference $(z-z')/z'$ versus the crossover exponent Δ, for both experiments and simulations. In this work, all values obtained, either experimentally or in simulations, for the crossover exponent are larger than unity. Therefore, we should obtain $z=z'$ (because $\Delta>1$) in all cases (except perhaps when $\Delta\geq 2$). This does not occur. However, it can be noted that $z\sim z'$ when $\Delta\sim 2$, since $z>z'$ when $\Delta<2$ and, reciprocally, $z<z'$ when $\Delta>2$. A striking result is the different behavior for experiments and simulations: the experimental data are situated in the region $\Delta<2$ and $z-z'>0$, while the data obtained in the numerical simulations are in the region $\Delta>2$ and $z-z'$ slightly above or below zero. This observation allows a qualitative interpretation based on the different predominant aggregation regimes for each set of data. If $z>z'$ that means that $S(t)$ grows faster than $l(t)$ [remember that $l(t)\sim N(t)^{-1}$]. This means that the most important contribution to the growth of $S(t)$ comes from the production of large clusters by aggregation of intermediate-size clusters. Hence, according to the interpretation of Eq. (10), $\Delta<2$ should be expected, in agreement with the experimental results. On the other hand, simulations show z roughly equal to z', so that in this case $\Delta=2$ should be expected. This does not happen because, for the simulations, the expression $\Delta=\omega/z$ also holds true and, while $z_{\text{sim}}\simeq z_{\text{expt}}$, ω_{sim} is considerably higher that ω_{expt}, giving $\Delta_{\text{sim}}\geq 2$.

In this work, no direct dependence of the exponent values on the control parameters λ or ϕ_{2D} has been observed. However, we have further checked whether the variability of Δ values might have its origin in the variation of the control parameters. In fact, we have studied the influence of two characteristic length scales R_1 and R_0, where R_1 is the distance at which the dipole-dipole interaction energy is equal

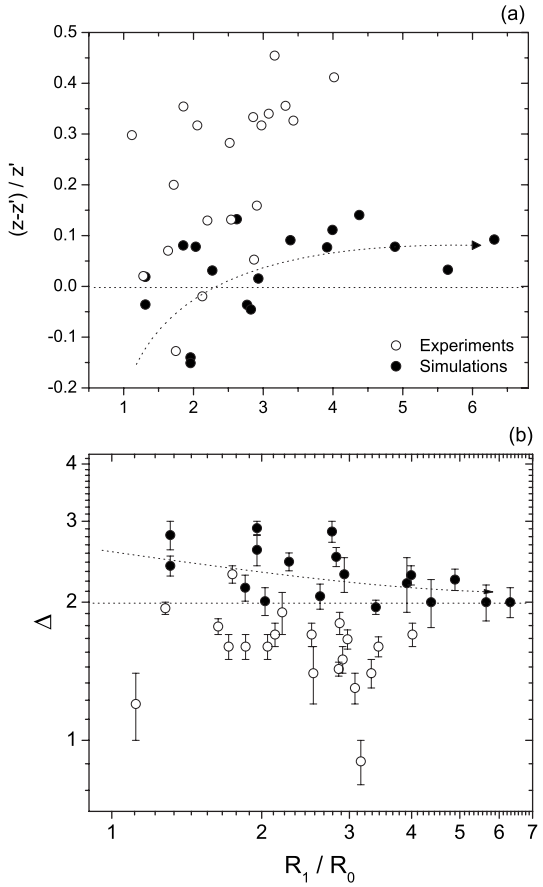

FIG. 11. Dependence of $(z-z')/z'$ (a) and Δ (b) on the ratio R_1/R_0 for experiments (open circles) and simulations (closed circles). The dotted line is a guide for the eye related to the apparent tendency to saturation in simulation data with high values of the ratio R_1/R_0.

to the energy of thermal fluctuations, i.e., $R_1 \equiv 2a\lambda^{1/3}$, and $R_0 \equiv \sqrt{\pi}a\phi_{2D}^{-1/2}$ represents the initial average interparticle distance. The ratio of these two length scales allows us to distinguish between diffusion-limited and field-driven aggregation processes. If, at the time the field is switched on, $R_1 < R_0$, the aggregation process should be diffusion limited, while if $R_1 > R_0$, the aggregation process should be field driven. Values for this ratio in experiments and simulations are quoted in Tables I and II, respectively.

In all of our experiments and simulation results, $R_1/R_0 > 1$ is verified. Therefore, from the beginning, the aggregation process should be dominated by the magnetic interaction among particles. However, a dependency on this ratio is found for the values of $(z-z')/z'$ and Δ (represented in Fig. 10), as can be seen in Figs. 11(a) and 11(b). In these figures, we can see how experimental and simulation results have different tendencies when the value of the ratio R_1/R_0 is increased. In Fig. 11(a), for the experimental data, the relative difference between the kinetic exponents tends to increase when R_1/R_0 grows; however, the data obtained by the simulations tend to a saturation value when $R_1/R_0 > 4$. A similar behavior can be observed in Fig. 11(b): the experimental values of the crossover exponent separate from the simulation values when the ratio grows. The crossover exponent values obtained in the simulations seem to converge to $\Delta \sim 2$ when $R_1/R_0 > 4$. The behavior shown in Figs. 12(a) and 12(b) for simulations at large values of R_1/R_0 is probably due to the dominance of the magnetic field attraction in the aggregation processes, which become less and less influenced by diffusion as R_1/R_0 increases.

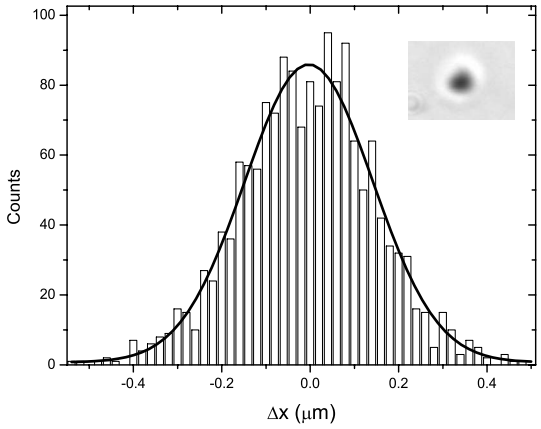

FIG. 12. Experimental determination by means of microrheology of the experimental diffusion coefficient D. We show the Gaussian fit to the number of counts obtained for each Δx. A Gaussian width 0.286 is obtained and therefore $D_x = 0.23 \pm 0.01$ $\mu m^2/s$ with $t = 45$ ms.

A remarkable difference between experiments and simulations is related to a characteristic aggregation time t_a that we might define as the time needed for half of the initial particles to become aggregated. Whereas in the experiment we have aggregation times $t_a \sim 10^2$ s, in the simulations we obtain $t_a \sim 0.1$ s. This difference might be at the origin of the low values of the exponent z reported in Ref. [22].

We can theoretically estimate the aggregation time for two magnetic particles under dipolar magnetic interaction using the equation of motion $\gamma\dot{r} + 3\pi^{-1}\mu\mu_0 m^2 r^{-4} = 0$. The result, depending on λ and ϕ_{2D}, is $t_{ag} \simeq 2a^2(15\lambda D)^{-1}\phi_{2D}^{-5/2}$ (for 3D aggregation, the exponent 5/2 must be replaced by 5/3). By means of this expression, we obtain aggregation times on the order of those obtained in the simulations for typical values of the external parameters. The cause of this discrepancy is not clear to us, although several possible mechanisms may be though of that have not been included in the theoretical model used in the simulations; for instance, effects of hydrodynamic interactions (particle-particle and/or particle-wall) on the diffusion coefficient of the clusters [47–49], or anomalous electrostatic interactions [50–52].

In order to clarify the role of the hydrodynamic interaction of the sedimented particles with the lower cell wall, we have performed some measurements by means of a microrheology technique [53]. In this technique, images captured with a constant time interval Δt are analyzed to follow the motion of the particles in the fluid. Then we calculate the displacement of the particle's center of mass. These displacements should show a Gaussian statistics with a width ω related to the particle's diffusion coefficient, so that $D = \omega^2/8t$. A typical experimental result, obtained with a time interval of $\Delta t = 45$ s, is shown in Fig. 12, which, after a Gaussian fit, yields $D_x = 0.23 \pm 0.01$ $\mu m^2/s$.

The height of the particle from the bottom window introduces a correction to the theoretical diffusion exponent for a free particle [43,54]. For a particle staying at a height of 1 μm above the bottom cell wall, the correction is $D/D_0 \approx 0.64$. Hence, using for D_0 the value estimated by means of the Einstein-Stokes relation ($D_0=0.343\ \mu m^2/s$) the corrected value for the diffusion coefficient is $D=0.23\ \mu m^2/s$, in perfect agreement with the experimental value. Anyway, this 30% decrease in the effective diffusion coefficient for a sedimented particle with respect to a nonsedimented one does not explain the large difference between the characteristic aggregation times found in experiments and simulations.

A final comment can be made about the lack of lateral aggregation events at large values of λ and large times. Many experimental results show that, at high values of λ and long aggregation times, lateral aggregation appears, which creates thicker structures, sometimes described as columns [55–59]. These lateral aggregation events appear because of a lateral attractive interaction between chains that may be caused either by fluctuations [38,60] or by the magnetic interaction between long chains [61]. However, experimental [62] and theoretical [61] work shows that this attractive lateral interaction between chains is much weaker than the longitudinal interaction that produces head-to-tail chain aggregation.

We would like to remark that lateral aggregation events are not observed in the experiments reported in this paper. Several physical mechanisms can conceivably be cooperating to prevent lateral aggregation. First of all, the particles have carboxylic groups in their surfaces, which, in an aqueous suspension, should give a negative surface charge to the particles, thus creating a repulsive electrostatic interaction among particles that is not high enough to preclude longitudinal aggregation, but might make more difficult the appearance of lateral aggregation, because of its comparative weakness.

Another factor is related to the sedimentation of the chains. Indeed, the force causing sedimentation is directly proportional to the volume of the aggregate [43]. Obviously, the volume of a chain of n particles is n times the volume of a particle. Hence, a chain of particles will certainly sink deeper than a single particle, which increases the hydrodynamic interaction with the bottom plate of the experimental cell. Moreover, recent results on numerical computations of the diffusion of chains close to a rigid wall [49] show that the reduction of the diffusion coefficient of a long chain close to a rigid surface can be very high. Therefore, in the conditions of the experiments of this paper, there must be a large hydrodynamic resistance to the lateral motion of the chains.

This may impede lateral aggregation in two ways. If the lateral attractive interaction were created by chain profile fluctuations, the reduced mobility of the particles due to the small distance to the cell bottom plate would decrease the amplitude of these fluctuations and, consequently, the lateral attractive interaction would be strongly reduced. If the lateral interaction were between long chains, these long sedimented chains would have a strongly reduced mobility and, consequently, lateral aggregation events between long sedimented chains should be very rare.

VI. CONCLUSIONS

The video-microscopy technique and image analysis have been used to obtain and process, respectively, experimental data on a sedimented magnetorheological suspension of 1-μm-diameter particles in water. Additionally, two-dimensional Brownian dynamics simulations have been developed to compare with the experimental results. We have shown that the Family-Vicsek scaling ansatz for the diffusion-limited cluster-cluster aggregation model is verified both in the experiments and in the numerical simulation results. We have obtained also different characteristic kinetic exponents by varying the external parameters λ and ϕ_{2D} (see Table I for experiments and Table II for simulations). The average exponents $\langle\beta\rangle_{expt}=0.43\pm0.02$ and $\langle z\rangle_{expt}\simeq\langle z\rangle_{sim}\simeq 0.6$ are in agreement with previous results found in the literature (the average values can be seen in Table III). However, discrepancies are observed in the rest of the exponents, especially for the crossover exponent values, verifying the relationship $1\leq\Delta_{expt}\leq 2\leq\Delta_{sim}\leq 3$. We noted how this result is correlated with the differences between kinetic exponent values, showing the predominance of different kinds of processes of aggregation for experiments and simulations. Furthermore, we found a dependence of the different values of Δ on the ratio R_1/R_0, exposing a dependency on the external parameters related to the magnetic field and the concentration of particles that deserves further investigation.

We have also shown a strong discrepancy between the characteristic particle-particle aggregation times in experiments and simulations. The origin of this discrepancy is not yet known. There is work in progress to study the electrostatic and hydrodynamic interactions of the experimental system, in order to understand the physical mechanism causing this discrepancy.

ACKNOWLEDGMENTS

We wish to acknowledge O. G. Calderón and P. L. Lucas for their work in previous versions of the BD code, J. M. González, J. M. Palomares, and F. Pigazo (ICMM) for the VSM magnetometry measurements, and P. Español for fruitful discussions, and J. C. Gómez Sáez for her correction of the English version of the manuscript. P.D.-G. has been supported by MEC. This research has been partially supported by MEC under Project No. FIS2006-12281-C02-02, and by CAM under Project No. S/0505/MAT/0227.

[1] J. Rabinow, AIEE Trans. **67**, 1308 (1948).
[2] W. M. Winslow, J. Appl. Phys. **20**, 1137 (1949).
[3] R. G. Larson, *The Structure and Rheology of Complex Fluids*, 1st ed. (Oxford University Press, NewYork, 1999).
[4] R. A. Kerr, Science **247**, 050401 (1990).
[5] Lord Corporation, http://www.lord.com/
[6] *Proceedings of the Sixth International Conference on ER and MR Fluids and Their Applications*, edited by M. Nakano and K. Koyama (World Scientific, Singapore, 1998).
[7] *Proceedings of the Seventh International Conference on ER and MR Fluids*, edited by R. Tao (World Scientific, Singapore, 2000).
[8] C. Wilhelm, F. Gazeau, and J. C. Bacri, Phys. Rev. E **67**, 061908 (2003).
[9] C. Wilhelm, J. Browaeys, A. Ponton, and J. C. Bacri, Phys. Rev. E **67**, 011504 (2003).
[10] C. Wilhelm, F. Gazeau, and J. C. Bacri, Europhys. News **3**, 89 (2005).
[11] A. K. Vuppu, A. A. García, S. K. Saha, P. E. Phelan, M. A. Hayes, and R. Calhoun, Lab Chip **4**, 201 (2004).
[12] A. K. Vuppu, A. A. García, M. A. Hayes, K. Booksh, P. E. Phelan, R. Calhoun, and S. K. Saha, J. Appl. Phys. **96**, 6831 (2004).
[13] R. Y. García, Ph.D. thesis, Arizona State University, 2003.
[14] P. Smirnov, F. Gazeau, M. Lewin, J. C. Bacri, N. Siauve, C. Vayssettes, C. A. Cuenod, and O. Clement, Magn. Reson. Med. **52**, 73 (2004).
[15] A. Egatz-Gómez, S. Melle, A. A. García, S. A. Lindsay, M. Márquez, P. Domínguez-García, M. A. Rubio, S. T. Picraux, J. L. Taraci, T. Clement, D. Yang, M. A. Hayes, and D. Gust, Appl. Phys. Lett. **89**, 034106 (2006).
[16] A. A. García, A. Egatz-Gómez, S. A. Lindsay, P. Domínguez-García, S. Melle, M. Márquez, M. A. Rubio, S. T. Picraux, D. Yang, P. Aella, M. A. Hayes, D. Gust, S. Loyprasert, T. Vázquez-Álvarez, and J. Wang, J. Magn. Magn. Mater. **311**, 238 (2007).
[17] T. Vicsek, *Fractal Growth Phenomena*, 2nd ed. (World Scientific, Singapore, 1992).
[18] S. Fraden, A. J. Hurd, and R. B. Meyer, Phys. Rev. Lett. **63**, 2373 (1989).
[19] A. T. Skjeltorp, Phys. Rev. Lett. **51**, 2306 (1983).
[20] G. Helgesen, A. T. Skjeltorp, P. M. Mors, R. Botet, and R. Jullien, Phys. Rev. Lett. **61**, 1736 (1988).
[21] G. Helgesen, P. Pieranski, and A. T. Skjeltorp, Phys. Rev. Lett. **64**, 1425 (1990).
[22] J. Cernak, G. Helgesen, and A. T. Skjeltorp, Phys. Rev. E **70**, 031504 (2004).
[23] G. Bossis, C. Mathis, Z. Minouni, and C. Paparoditis, Europhys. Lett. **11**, 133 (1990).
[24] M. Fermigier and A. P. Gast, J. Colloid Interface Sci. **154**, 522 (1992).
[25] J. C. Bacri, K. Djerfi, and S. Neveu, J. Magn. Magn. Mater. **123**, 67 (1993).
[26] J. Promislow, A. P. Gast, and M. Fermigier, J. Chem. Phys. **102**, 5492 (1995).
[27] S. Melle, M. A. Rubio, and G. G. Fuller, Phys. Rev. Lett. **87**, 115501 (2001).
[28] T. Vicsek and F. Family, Phys. Rev. Lett. **52**, 1669 (1984).
[29] T. A. Witten and L. M. Sander, Phys. Rev. Lett. **47**, 1400 (1981).
[30] P. Meakin, Phys. Rev. Lett. **51**, 1119 (1983).
[31] M. Kolb, R. Botet, and R. Jullien, Phys. Rev. Lett. **51**, 1123 (1983).
[32] P. Meakin, T. Vicsek, and F. Family, Phys. Rev. B **31**, 564 (1985).
[33] M. Carmen Miguel and R. Pastor-Satorras, Phys. Rev. E **59**, 826 (1999).
[34] *Proceedings of the Ninth International Conference on ER Fluids and MR Suspensions*, edited by K. Lu, R. Shen, and J. Liu (World Scientific, Singapore, 2005).
[35] J. Cernak, P. Macko, and M. Kasparkova, J. Phys. D **24**, 1609 (1991).
[36] J. Cernak, J. Magn. Magn. Mater. **132**, 258 (1994).
[37] D. Sohn, J. Magn. Magn. Mater. **173**, 305 (1997).
[38] J. E. Martin, J. Odinek, and T. C. Halsey, Phys. Rev. Lett. **69**, 1524 (1992).
[39] M. von Smoluchowski, Z. Phys. Chem., Stoechiom. Verwandtschaftsl. **92**, 129 (1917).
[40] S. Miyazima, P. Meakin, and F. Family, Phys. Rev. A **36**, 1421 (1987).
[41] S. H. Gee, Y. K. Hong, D. W. Erickson, M. H. Park, and J. C. Sur, J. Appl. Phys. **93**, 7560 (2003).
[42] S. Melle, O. G. Calderón, M. A. Rubio, and G. G. Fuller, J. Non-Newtonian Fluid Mech. **102**, 135 (2002).
[43] L. P. Faucheux and A. J. Libchaber, Phys. Rev. E **49**, 5158 (1994).
[44] U. S. National Institutes of Health, http://rsb.info.nih.gov/ij/
[45] D. J. Klingenberg, F. Swol, and C. F. Zukovski, J. Chem. Phys. **91**, 7888 (1989).
[46] M. Mohebi, N. Jamasbi, and J. Liu, Phys. Rev. E **54**, 5407 (1996).
[47] M. M. Tirado and J. G. de la Torre, J. Chem. Phys. **71**, 2581 (1979).
[48] M. M. Tirado and J. G. de la Torre, J. Chem. Phys. **73**, 1986 (1980).
[49] R. Kutteh, J. Chem. Phys. **119**, 9280 (2003).
[50] S. H. Behrens and D. G. Grier, J. Chem. Phys. **115**, 6716 (2001).
[51] Y. Han and D. G. Grier, Phys. Rev. Lett. **91**, 038302 (2003).
[52] D. G. Grier and Y. Han, J. Phys.: Condens. Matter **16**, S4145 (2004).
[53] T. G. Mason and D. A. Weitz, Phys. Rev. Lett. **74**, 1250 (1995).
[54] T. Benesch, S. Yiacoumi, and C. Tsouris, Phys. Rev. E **68**, 021401 (2003).
[55] E. Lemaire, Y. Grasselli, and G. Bossis, J. Phys. II **2**, 359 (1992).
[56] R. Tao, Phys. Rev. E **47**, 423 (1993).
[57] S. Cutillas, G. Bossis, and A. Cebers, Phys. Rev. E **57**, 804 (1998).
[58] M. F. Islam, K. H. Lin, D. Lacoste, T. C. Lubensky, and A. G. Yodh, Phys. Rev. E **67**, 021402 (2003).
[59] C. Metayer, V. A. Sterligov, A. Meunier, G. Bossis, J. Persello, and S. V. Svechnikov, J. Phys.: Condens. Matter **16**, S3975 (2004).
[60] T. C. Halsey and W. Toor, Phys. Rev. Lett. **65**, 2820 (1990).
[61] M. Gross and S. Kiskamp, Phys. Rev. Lett. **79**, 2566 (1997).
[62] E. M. Furst and A. P. Gast, Phys. Rev. E **62**, 6916 (2000).